Atmos. Meas. Tech. Discuss., https://doi.org/10.5194/amt-2019-98
Manuscript under review for journal Atmos. Meas. Tech.
Discussion started: 14 March 2019

Atmospheric Measurement Techniques Discussions

Dust mass, CCN, and INP profiling with polarization lidar: Updated POLIPHON conversion factors from global AERONET analysis

Albert Ansmann[1], Rodanthi-Elisavet Mamouri[2], Julian Hofer[1], Holger Baars[1], Dietrich Althausen[1], and Sabur F. Abdullaev[3]

[1]Leibniz Institute for Tropospheric Research, Leipzig, Germany
[2]Cyprus University of Technology, Dep. of Civil Engineering and Geomatics, Limassol, Cyprus
[3]Physical Technical Institute, Academy of Sciences of the Republic of Tajikistan, Dushanbe, Tajikistan

Correspondence to: A. Ansmann
(albert@tropos.de)

Abstract. The POLIPHON (Polarization Lidar Photometer Networking) method permits the retrieval of particle number, surface area, and volume concentration for dust and non-dust aerosol components. The obtained microphysical properties are used to estimate height profiles of particle mass, cloud condensation nucleus (CCN) and ice-nucleation particle (INP) concentrations. Of central importance is the conversion of the lidar-derived extinction profiles into aerosol miccrophysical properties (number, surface area, volume). These conversion parameters are determined from Aerosol Robotic Network (AERONET) aerosol climatologies of optical and microphysical properties. In this article we focus on the dust-related POLIPHON retrieval and present an updated set of dust conversion factors considering all relevant deserts around the globe. We apply the new conversion factor set to a dust measurement with polarization lidar in Dushanbe, Tajikistan, in central Asia. Strong aerosol layering was observed with mineral dust advected from Kazakhstan (0-2 km height), Iran (2-5 km), the Arabian peninsula (5-7 km), and the Sahara (8-10 km). POLIPHON results obtained with different sets of conversion parameters were contrasted and discussed in terms of uncertainties.

1 Introduction

Increasing urbanization, rising aerosol pollution levels, and the need for an improved understanding of the relationship between aerosols, clouds, and precipitation to reduce the high uncertainties in future climate predictions motivated us to develop a robust and easy-to-handle lidar method for an height-resolved retrieval of particle mass concentration and cloud-relevant parameters such as cloud condensation nucleus (CCN) and ice-nucleating particle (INP) concentrations (Mamouri and Ansmann, 2016, 2017). Lidar is the only available technique for continuous monitoring and vertical profiling of local and regional aerosol conditions (Baars et al., 2016) and of intercontinental long-range aerosol transport in the free troposphere and lower stratosphere (Ansmann et al., 2018; Haarig et al., 2018). The recently introduced POLIPHON (Polarization Lidar Photometer Networking) technique allows the requested aerosol monitoring of environment and climate-relevant aerosol properties. The method combines the unique features of polarization lidar (see, e.g., Freudenthaler et al., 2009; Tesche et al., 2011), permitting an accurate separation of dust from aerosol pollution optical properties, with the unique global aerosol climatology of aerosol optical and

Atmos. Meas. Tech. Discuss., https://doi.org/10.5194/amt-2019-98
Manuscript under review for journal Atmos. Meas. Tech.
Discussion started: 14 March 2019

Atmospheric Measurement Techniques Discussions

microphysical properties provided by AERONET (Aerosol Robotic Network) (Holben et al., 1998). The POLIPHON method can be applied to observations with wide-spread ground-based single-wavelength polarization lidars (Cordoba-Jabonero et al., 2018) as well as to spaceborne single-wavelength polarization lidar measurements with CALIOP (Cloud-Aerosol Lidar Observations with Orthogonal Polarization) (Winker et al., 2009; Mamouri and Ansmann, 2015; Marinou et al., 2017, 2018) and ATLID (Atmospheric Lidar) of the EarthCARE (Earth Clouds, Aerosol, and Radiation Experiment) mission (Illingworth et al., 2015). The new approach has successfully been tested and compared with in situ measured vertical profiles of particle mass concentration (Mamali al., 2018), CCN (Düsing et al., 2018), and INP concentration (Schrod et al., 2017; Marinou et al., 2018).

In this article, we further improve and extend the POLIPHON method towards a global application in the case of mineral dust monitoring. This effort is triggered by several reasons: First of all, mineral dust is a global player in the climate system by sensitively influencing the radiative transfer in the Earth atmosphere and by serving as an important reservoir for favorable INPs (Hoose and Möhler, 2012; Murray et al., 2012; Kanji et al., 2017) which can initiate ice and precipitation formation already at high temperatures of -15 to -35°C. Without aerosol particles ice and rain formation rates would be strongly reduced in the atmosphere. However, and this is the second reason for the dust-related improvements presented here, POLIPHON has only be applied to Saharan dust observations yet. The technique is based on the conversion of lidar-derived particle extinction coefficients into microphysical properties and needs respective conversion factors, and these have been determined for Saharan dust only. Now the questions arise: Are these Saharan dust conversion factors valid for the different dust regimes around the globe? Do we need different sets of conversion factors for, .e.g., Saharan dust, Middle East dust, East Asian dust, dust in North and South America, South Africa, and Australia? Or can we develop one set of globally valid dust conversion factors to facilitate the use of the POLIPHON method especially in spaceborne lidar applications? Guided by these questions we studied the AERONET data base in large detail. The study was also motivated by the growing PollyNET (POrtabLe Lidar sYstem NETwork) activities (Baars et al., 2016; Engelmann et al., 2016). Meanwhile, long-term observations are available, e.g., for Greece and Cyprus, Israel and United Arab Emirates, Tajikistan and South Korea, and recently also for southern Chile. Many cruises across the Atlantic from northern Germany to South Africa or South America with a Polly aboard the Research Vessel Polarstern have been conducted in addition (Kanitz et al., 2013; Bohlmann et al., 2018).

The paper is organized as follows. A brief overview of the POLIPHON methodology is given in Sect. 2. In this article, the focus is on mineral dust, especially on the determination of dust conversion factors from worldwide AERONET observations. These conversion parameters are needed to convert lidar profiles of dust extinction coefficients into microphysical properties of dust. The results of the in-depth AERONET data analysis are presented in Sect. 3. We analyzed long-term sun/sky photometer observations of 21 AERONET sites in or close to important mineral dust source regions around the world (AERONET, 2019). In Sect. 4, we present a case study of a Polly observation at Dushanbe, Tajikistan, with mineral dust up to the tropopause advected from central Asia (at heights below 2 km above ground), from Iran and the Arabia peninsula (2–7 km height range), and the Sahara (above about 8 km height). The case study is used to demonstrate the full potential of the POLIPHON method for mineral dust profiling with the updated AERONET-based conversion factors and also to provide insight into the uncertainties in the POLIPHON products when using different sets of conversion parameters (obtained from the AERONET data analysis for different desert regions). Concluding remarks are given in Sect. 5.

Atmos. Meas. Tech. Discuss., https://doi.org/10.5194/amt-2019-98
Manuscript under review for journal Atmos. Meas. Tech.
Discussion started: 14 March 2019

Atmospheric Measurement Techniques Discussions

2 Methodological background

The POLIPHON method is described in detail in Mamouri and Ansmann (2014, 2016, 2017). The main part of the POLIPHON data analysis deals with the conversion of aerosol-type-resolved particle extinction coefficients into respective particle microphysical properties. Table 1 provides an overview of POLIPHON dust products and the respective conversions. Similar conversions for non-dust aerosols such as maritime particles or continental fine-mode aerosol pollution (urban haze, biomass burning smoke) can be found in Mamouri and Ansmann (2016, 2017).

According to Table 1 the POLIPHON data analysis allows us to derive height profiles of dust mass concentrations M_{d} from the dust extinction coefficients σ_{d}, also separately for coarse dust (M_{dc} considering particles with radius>500 nm) and fine dust (M_{df} considering dust particles with radius<500 nm) from respective coarse and fine dust extinction coefficients σ_{dc} and σ_{df}. In the first step, the dust extinction coefficients are converted into dust particle volume concentrations v_d, v_{dc}, and v_{df} and, in the second step, the volume concentrations are multiplied by the dust particle density ρ_{d} of 2.6 $\mathrm{g/cm^{-3}}$ (Ansmann et al., 2012) to obtain the dust mass concentrations. Further POLIPHON conversion products listed in Table 1 are needed to estimate cloud-relevant aerosol parameters such as the cloud condensation nucleus concentration (CCNC) and ice-nucleating particle concentration (INPC). The number concentrations $n_{100,\mathrm{d}}$ (considering particles with radius >100 nm) is a good estimation for dust CCNC (Mamouri and Ansmann, 2016; Lv et al., 2018) for a frequently occurring and thus typical water supersaturation of 0.2% (Siebert and Shaw, 2017). For 0.2% supersaturation, $f_{\mathrm{ss,d}}$ is therefore 1.0 in Table 1. The particle number concentration $n_{250,\mathrm{d}}$ (considering particles with radius >250 nm) and the dust particle surface area concentration s_{d} are input in the estimation of height profiles of INPC (DeMott et al., 2010; DeMott et al., 2015; Niemand et al., 2012; Ullrich et al., 2017). Further input in the INPC retrieval are the temperature profile $T(z)$ and an assumed ice super saturation value S_{ICE} in the case of deposition-freezing INPC (Ullrich et al., 2017). All this is described in detail in Mamouri and Ansmann (2016, 2017). More details to the INPC retrieval are also given in Sect. 4.

The uncertainties in the POLIPHON retrieval products are 20-30% for M_{d}, $n_{250,\mathrm{d}}$, and s_{d}, a factor of two to three for $n_{100,\mathrm{d}}$ and n_{CCN}, and an order of magnitude for $n_{\mathrm{INP,d}}$ (Mamouri and Ansmann, 2016, 2017). Uncertainties will be discussed in detail in Sect. 5.

The retrieval of trustworthy conversion factors from AERONET observations is of central importance for the applicability of the POLIPHON method. We use the example of mass concentration retrieval to explain the derivation of the conversion factors from the AERONET data base. The mass concentration is given by

$$M_i(z) = \rho_i \times v_i(z) \tag{1}$$

with the mass concentration M_i for aerosol type i, the particle density ρ_i for the specific aerosol type i, and the particle volume concentration v_i. In the POLIPHON method, we distinguish marine aerosol (i = m), mineral dust (i = d, df, dc for total dust, fine-mode dust, and coarse-mode dust, respectively) and continental aerosol pollution such as urban haze and biomass burning smoke (i = c). The particle volume concentration can be obtained from the following conversion:

$$v_i(z) = c_{\mathrm{v},i,\lambda} \times \sigma_{i,\lambda}(z) \tag{2}$$

Atmos. Meas. Tech. Discuss., https://doi.org/10.5194/amt-2019-98
Manuscript under review for journal Atmos. Meas. Tech.
Discussion started: 14 March 2019

Atmospheric Measurement Techniques Discussions

with the conversion factor $c_{\mathrm{v},i,\lambda}$ and the particle extinction coefficient $\sigma_{i,\lambda}$ measured with lidar at wavelength λ. The conversion factor is obtained from the vertically integrated particle volume concentration V_i (denoted as column volume concentration) and the aerosol optical thickness (AOT) denoted as $\tau_{i,\lambda}$, stored in the AERONET data base (AERONET, 2019),

$$c_{\mathrm{v},i,\lambda} = \frac{V_i}{\tau_{i,\lambda}}\,. \tag{3}$$

To provide a link to the lidar-derived height profile of $\sigma(z)$ (see Eq. 2), we introduce an aerosol layer depth with an arbitrarily chosen vertical extent D. With D, Eq. (3) can be written as

$$c_{\mathrm{v},i} = \frac{V_i/D}{\tau_{i,\lambda}/D} = \frac{v_i}{\sigma_{i,\lambda}} \tag{4}$$

with the layer mean volume concentration v_i for aerosol type i and the layer mean particle extinction coefficient $\sigma_{i,\lambda}$. For simplicity, we assume that all aerosol is confined to the introduced layer with constant depth D. We may interprete this layer as the polluted boundary layer with depth D or as a lofted dust layer with a vertical extent D. The introduction of D has no impact on the further retrieval of the conversion factors. The layer is only introduced to move from column-integrated values and AOT to more lidar-relevant quantities like concentrations and extinction coefficients.

In this study here, we focus on mineral dust (i = d, df, dc) and a polarization lidar transmitting laser pulses at λ=532 nm. We omit the wavelength index in the following. Then we can write for the conversion factor, e.g., in the case of total (fine + coarse) dust,

$$c_{\mathrm{v,d}} = \frac{v_{\mathrm{d}}}{\sigma_{\mathrm{d}}}\,. \tag{5}$$

To obtain a climatologically representative dust conversion factor for a given AERONET station, we selected all dust-dominated observations (from number $j = 1$ to J_{d} collected over many years) defined by an Ångström exponent AE<0.3 and 532 nm AOT>0.1. For each dust observation j we computed $c_{\mathrm{v,d},j}$ and determined the mean value which best represents the required conversion factor,

$$c_{\mathrm{v,d}} = \frac{1}{J_{\mathrm{d}}}\sum_{j=1}^{J_{\mathrm{d}}}\frac{v_{\mathrm{d},j}}{\sigma_{\mathrm{d},j}}\,. \tag{6}$$

In the same way, all other conversion parameters in Table 1 are computed:

$$c_{\mathrm{v,dc}} = \frac{1}{J_{\mathrm{d}}}\sum_{j=1}^{J_{\mathrm{d}}}\frac{v_{\mathrm{df},j}}{\sigma_{\mathrm{d},j}}\,, \tag{7}$$

$$c_{\mathrm{v,df}} = \frac{1}{J_{\mathrm{d}}}\sum_{j=1}^{J_{\mathrm{d}}}\frac{v_{\mathrm{dc},j}}{\sigma_{\mathrm{d},j}}\,, \tag{8}$$

$$c_{250,\mathrm{d}} = \frac{1}{J_{\mathrm{d}}}\sum_{j=1}^{J_{\mathrm{d}}}\frac{n_{250,\mathrm{d},j}}{\sigma_{\mathrm{d},j}}\,, \tag{9}$$

$$c_{\mathrm{s,d}} = \frac{1}{J_{\mathrm{d}}}\sum_{j=1}^{J_{\mathrm{d}}}\frac{s_{\mathrm{d},j}}{\sigma_{\mathrm{d},j}}\,. \tag{10}$$

Atmos. Meas. Tech. Discuss., https://doi.org/10.5194/amt-2019-98
Manuscript under review for journal Atmos. Meas. Tech.
Discussion started: 14 March 2019

Atmospheric Measurement Techniques Discussions

In Mamouri and Ansmann (2016), we explain how we calculate $n_{250,\mathrm{d},j}$, $s_{\mathrm{d},j}$ as well as $n_{100,\mathrm{d},j}$ (discussed below) from the downloaded AERONET size distribution data sets. The volume concentrations $v_{\mathrm{d},j}$, $v_{\mathrm{dc},j}$, and $v_{\mathrm{df},j}$ are given as numbers in the AERONET data base.

In the retrieval of the conversion parameters required to obtain $n_{100,\mathrm{d}}$, we used a different approach. Following the procedure suggested by Shinozuka et al. (2015), we applied a log-log regression analysis to the $\log(n_{100,\mathrm{d}})$-$\log(\sigma_{\mathrm{d}})$ data field for each of the considered 21 AERONET station and determined in this way representative values for $c_{100,\mathrm{d}}$ and x_{d} that fulfill best the relationship,

$$\log\left(n_{100,\mathrm{d}}\right) = \log\left(c_{100,\mathrm{d}}\right) + x_{\mathrm{d}} \log\left(\sigma_{\mathrm{d}}\right), \tag{11}$$

as will be shown in the next section.

For completeness, it remains to be mentioned that the dust-case-selecting Ångström exponent AE describes the AOT wavelength dependence in the spectral range from 440-870 nm and is given in the AERONET data base together with 500 nm AOT. The dust AOT is dominated by coarse dust particles and is almost wavelength-independent, i.e., AE is close to zero. In our correlation study we use the AOT for the laser wavelength of 532 nm. The 532 nm AOT τ_{532} is obtained from the 500 nm AOT τ_{500} and the Ångström exponent a by

$$\tau_{532} = \tau_{500}(500/532)^{a}\,. \tag{12}$$

3 Conversion parameters from the AERONET data base

Table 2 contains the list of AERONET stations considered in our effort to determine dust conversion factors for different desert regions around the globe. We preferred stations with long data records and large numbers of observations. As can be seen in Table 2, the number of useful dust observations (AE<0.3, AOT>0.1) ranges from 218–4199 for 13 out of the 21 sites and is thus sufficiently high enough for the statistical analysis. The first six stations (from Tamanrasset to Ilorin) in Table 2 are exclusively influenced by Saharan dust, the next six stations (Limassol to Mezaira) by Saharan and Middle East (mainly Arabian desert) dust, followed by three stations in Central and East Asia (Dushanbe to Dalanzadgad), which are influenced by long-range transport from Sahara and western Asian deserts (including deserts in Iran and Kazakhstan) but also strongly by desert dust from Taklamakan and Gobbi deserts (Langzhou, Dalanzadgad). Sun photometer observations in North America (Great Basin, Tuscon, White-Sands), South America (Patagonian desert, Trelew), South Africa (Kalahari desert, Gobabeb) and in the central Australian desert (Birdsville) complete our global AERONET dust data set. We added the Leipzig AERONET observations with a small number of strong Saharan dust outbreaks.

3.1 Correlations between $n_{250,d}$, s_{d}, and v_{d} with dust extinction coefficient σ_{d}

Figure 1 provides an overview of the relationship between the dust particle number concentration of larger particles $n_{250,\mathrm{d}}$ and the dust extinction coefficient σ_{d} in (a), dust particle surface area concentration s_{d} and σ_{d} in (b), and between the dust volume concentration v_{d} and σ_{d} in (c). Twelve different AERONET stations are considered in the figure. The mean conversion factors

Atmos. Meas. Tech. Discuss., https://doi.org/10.5194/amt-2019-98
Manuscript under review for journal Atmos. Meas. Tech.
Discussion started: 14 March 2019

Atmospheric Measurement Techniques Discussions

$c_{250,\mathrm{d}}$ (Eq. 9), $c_{\mathrm{s,d}}$ (Eq. 10), and $c_{\mathrm{v,d}}$ (Eq. 6) are indicated as straight lines (regression lines) for the Saharan dust stations of Sal, Cabo Verde (a), Dakar, Senegal (b), and Tamanrasset, Algeria (c).

We set the layer depth D in Eq. (4) simply to 1000 m so that an easy conversion of the σ_{d} values into the original AERONET AOT values is possible by dividing σ_{d} (in Mm^{-1}) by 1000. We selected different colors to distinguish Saharan dust observations (green), Middle East measurements (orange) and data collected in Central and East Asia (red). We used bluish colors (blue, cyan) for the American and Australian stations, respectively, and blue-green for the African site (in the southern hemisphere) of Gobabeb.

As can be seen in Fig. 1, there are no large differences in the correlation features for the different desert regions. However, some red and orange clusters are visible in (a) and (c) and later on in the calculated conversion factors for all stations presented and discussed in Sect. 3.4. However, the given Saharan dust conversion factors in (a) for Cabo Verde (based on 2982 data points), in (b) for Dakar, Senegal (3823 data points), and in (c) for Tamanrasset, Algeria (3542 data points) characterize already very well the main relationship between the shown microphysical and optical parameters for the different dust regions.

The spread in the data mainly reflects variations in the dust aerosol characteristics (size distribution, refractive index) as a function of varying mixtures of freshly emitted local dust and long-range-transported aged dust. The different dust types and mixtures may occur in different layers above each other (as in the case study in Sect. 4). Furthermore, even in the case of dominating dust with AE<0.3, an influence of local and regional aerosol pollution on the sun photometer observations cannot fully be excluded. Uncertainties in the AERONET data inversion procedure applied to obtain the microphysical properties from the measured AOT and sky radiance observations may have also contributed to the scatter in the data. The scatter provides an impression of the overall uncertainty in the determined conversion factors and thus in the POLIPHON products. However, it should also be mentioned that dust extinction coefficients in lofted layers above the boundary layer (in the free troposphere) seldom exceed 200-300 Mm^{-1}. For the σ_{d} <500 Mm^{-1} the scatter in the data is comparably low in Fig. 1.

3.2 Relationship between $n_{100,d}$ and dust extinction coefficient σ_{d}

A different way of the data analysis is used for $n_{100,\mathrm{d}}$. As suggested by Shinozuka et al. (2015) we correlated $\log(n_{100,\mathrm{d}})$ vs $\log(\sigma_{\mathrm{d}})$. Figure 2 shows the relationship between particle number concentration $n_{100,\mathrm{d}}$ and the dust extinction coefficient σ_{d} at 532 nm for two stations (Mezaira, Dushanbe) in logarithmic scale. As outlined in Sect. 2, the particle number concentration $n_{100,\mathrm{d}}$, considering only the particles with dry radius >100 nm, represents very well the CCN reservoir in the case of dust particles (Mamouri and Ansmann, 2016; Lv et al., 2018).

In Fig. 2, we highlight the difference in the correlation when using all available data (532 nm dust AOT from 0.1 to 3.0 or σ_{d} from 100-3000 Mm^{-1}) and when using only observations with AOT<0.6 for the two stations of Mezaira and Dushanbe. By detailed inspection of all data sets (station by station), we observed that the correlation strength significantly decreases with increasing AOT and is no longer clearly visible for all measurements with AOT from 1.0 to 3.0. The Dushanbe data set shown in Fig. 2b is a good example for this observation in the majority of sites.

We can only speculate about the reason for the weak relationship for AOT>0.6. When the AOT is large, the coarse-mode dust fraction may control the measured optical properties and respective inversion results so much that a trustworthy retrieval

Atmos. Meas. Tech. Discuss., https://doi.org/10.5194/amt-2019-98
Manuscript under review for journal Atmos. Meas. Tech.
Discussion started: 14 March 2019

Atmospheric Measurement Techniques Discussions

of the small particle fraction with radii from, e.g., 100–200 nm is no longer possible. Another explanation is that at high AOT conditions, the amount of the fine dust particles may vary just randomly. It is also possible that the AERONET observations themselves cause problems. Most inversion computations are based on observations in the early morning and evening hours when the effective impact of aerosols is strongest (so that the effective dust AOT is even higher by a factor of two and more than the one for the vertical column stored in the AERONET data base). At these low-visibility conditions, the short-wavelength channels (340 and 380 nm) may have problems to correctly measure the overall AOT (Rayleigh AOT plus particle AOT). The short-wavelength AOT values are, however, most sensitive to the optical properties of small dust particles and thus have a strong influence on the accuracy in the $n_{100,\mathrm{d}}$ retrieval.

As a consequence of the low correlation between $\log(n_{100,\mathrm{d}})$ and $\log(\sigma_{\mathrm{d}})$ for large AOT we restricted the determination of the conversion parameters $c_{100,\mathrm{d}}$ and x_{d} (see Eq. 11) by means of a regression analysis to AOT values from 0.1-0.6 (or respective σ_{d} from 100-600 Mm^{-1}).

Figure. 3 provides further inside into the correlation between $\log(n_{100,\mathrm{d}})$ and $\log(\sigma_{\mathrm{d}})$. Observations for different stations influenced by Saharan, Middle East, central Asian, American, and Australian dust are shown. The Saharan dust data set collected at Cabo Verde belongs to the few data sets (out of the 21 AERONET stations) with a likewise good correlation between $\log(n_{100,\mathrm{d}})$ and $\log(\sigma_{\mathrm{d}})$ even for large extinction values >600 Mm^{-1} and corresponding AOT values >0.6. In Fig. 3, regression analysis results (in accordance with Eq. 11) for Mezaira and Cabo Verde are compared. Furthermore, the relationship between $n_{100,\mathrm{d}}$ and σ_{d} as found by Shinozuka et al. (2015) for dusty field sites is presented.

As mentioned above, most of the dust-related lidar observations in the free troposphere show dust extinction coefficients (σ_{d}) <200-300 M^{-1}. For a moderate dust extinction value of 100 Mm^{-1}, the POLIPHON retrieval yields $n_{100,\mathrm{d}} \approx 150$ cm^{-3}, 250 cm^{-3}, and 350 cm^{-3} when using $c_{100,\mathrm{d}}$ and x_{d} numbers as derived from the Cabo Verde and Mezaira AERONET observations (AOT<0.6) and by using the Shinozuka parameterization, respectively. Thus, an overall error of a factor 2-3 as concluded by Shinozuka et al. (2015) and corroborated by Mamouri and Ansmann (2016) is justified in the estimation of $n_{100,\mathrm{d}}$ and the respective CCNC profiles.

3.3 Overview of AERONET-derived conversion parameters

In Table 3, the AERONET-based conversion parameters for all stations are presented. Regional, continental, and global mean sets of conversion parameters are given as well. Figures 4 and 5 provide a station-by-station overview of the conversion parameters. Systematic differences from region to region are visible in the case of $c_{250,\mathrm{d}}$ and also weakly for $c_{\mathrm{v,d}}$. The conversions parameters for the American, Australia, and southern Africa need to be handled with caution because the number of available observations is relatively low and the mean 532 nm AOT of these observations was low as well with values from 0.15–0.25. A decrease in $c_{250,\mathrm{d}}$ and a slight increase in $c_{\mathrm{v,d}}$ (and $c_{\mathrm{v,dc}}$) from African to East Asian AERONET stations suggests that, for the same measured extinction coefficient (σ_{d}), the accumulation mode particle number concentration (in our case particles with radius from 250–500 nm) is slightly larger and the coarse mode dust particle number concentration, dominating the dust volume concentration, is lower in the case of Saharan dust compared to East Asian dust. This behavior may indicate that the African AERONET stations, e.g., in Cabo Verde, Izana, and Dakar observe predominantly dust after long-range transport

Atmos. Meas. Tech. Discuss., https://doi.org/10.5194/amt-2019-98
Manuscript under review for journal Atmos. Meas. Tech.
Discussion started: 14 March 2019


Atmospheric Measurement Techniques Discussions

(which leads to a bit enhanced fine dust fraction because of size dependent sedimentation and removal of particles), whereas the East Asian AERONET stations may be influenced more frequently by the occurrence of local, freshly emitted dust with the relatively strong contribution of coarse-mode particles. Similar conditions as suggested for Central and East Asia may hold for the American and Australian stations.

The smooth but steady changes in $c_{250,\mathrm{d}}$ and $c_{\mathrm{v,d}}$ from the Saharan, over the Middle East to the central and eastern Asian AERONET stations probably indicates that the Middle East stations are influenced by both, local, western Asian dust sources (mostly Arabian dust) and Saharan dust (with the prevailing westerly winds). Only the African stations and the East Asian stations at Lanzhou and Dalanzadgad are clearly separated and allow to contrast dust properties of African and Asian deserts. All in all, the observed regional differences in the dust conversion parameters in Fig. 4 are small and of the order of $\pm$15-20% for most of the parameters and stations.

Fig. 5 provides a summarizing overview of the final results for $c_{100,\mathrm{d}}$ and x_{d}. Because of the large scatter in the log-log data fields expressed in the large uncertainty bars in the figure we can only give recommendations regarding the selection of the most reasonable set of dust conversion parameters. For the extinction exponent x_{d} a value of 0.80 seems to be appropriate. This exponent is then linked to $c_{100,\mathrm{d}}$ values of 5–6 cm^{-1} (at σ_{d} =1 Mm^{-1}).

4 Lidar measurement example: Case study of a dust observation in Tajikistan

We applied the updated new set of conversion parameters to a dust measurement with our Polly lidar at Dushanbe (38.6°N, 68.9°E, 820 m a.s.l.), Tajikistan, in April 2015. The lidar observations were performed in the framework of an 18-month field campaign CADEX (Central Asian Dust Experiment) (Hofer et al., 2017). The full potential of the POLIPHON method (Table 1) will be shown in this section, with focus on the impact of the elected conversion factors on the results and related uncertainties. The case presented here was already discussed in terms of optical properties by Hofer et al. (2017).

Figure 6 presents an overview of the aerosol conditions observed with lidar on 13 April 2015. A pronounced dust layer was detected between 2 and 5 km height (above ground level, AGL, about 3-6 km height above sea level, a.s.l.). Dust was observed up to cirrus heights. The AERONET sun photometer observations at Dushanbe showed a 500 nm AOT of 0.4, AE of 0.2, and a fine-mode fraction (FMF) of 0.2 (just before sunset close to 13:00 UTC). Thus, fine dust contributed about 20% to the overall (fine and coarse) dust extinction coefficient. According to the backward trajectories in Fig. 7a, mineral dust in the polluted boundary layer (0-2 km height) originated from Kazakhstan and local dust sources. The dust particles in the thick dust layer from to 2–5 km height were mostly emitted in Iran and Oman. Higher up (above 5 km) long range transport of dust from the Arabian peninsula (5-7 km height) and even the Sahara (8-10 km) prevailed. As can be seen in Fig. 7b, according to the forward trajectories the dust was advected towards eastern China. This case study documents that not only Asian but also African and Middle East dust can influence the dust conditions over China, Korea, and Japan.

Figure 8a shows the basic lidar profiles used in the POLIPHON data analysis. The height profiles of the particle (dust + non-dust) backscatter coefficient and the related particle linear depolarization ratio are used to derive dust and non-dust extinction profiles (Mamouri and Ansmann, 2014, 2017). The dust extinction coefficients are then converted into the dust mass concen-

Atmos. Meas. Tech. Discuss., https://doi.org/10.5194/amt-2019-98
Manuscript under review for journal Atmos. Meas. Tech.
Discussion started: 14 March 2019

trations in Fig. 8b by means the dust conversion factor $c_{\mathrm{v,d}}$ in Table 3 for Dushanbe, but also by using the conversion factor for Cabo Verde to show the impact of the selected conversion factor on the POLIPHON end product. The mass computation is performed in the way described in Table 1. The corresponding dust mass fraction (ratio of dust mass concentration to total particle mass concentration) is presented in Fig. 8b as well. The two mass conversion factors for Dushanbe and Cabo Verde represent a relatively high and low value of all conversion factors listed in Table 3. The differences in the POLIPHON results caused by using the different conversion factors are well covered by the overall uncertainty in the POLIPHON mass retrieval of 30% (see the error bars in Fig. 8) which also includes the uncertainty in the dust extinction determination.

Figure 9 presents the POLIPHON results in terms of several CCNC profiles obtained with conversion parameter sets for Cabo Verde, Mezaira, and Dushanbe (see Table 3). As mentioned, $n_{\mathrm{CCN,d}} \approx n_{100,\mathrm{d}}$ for a water supersaturation of 0.2%. Such a weak supersaturation typically occurs when air parcels are lifted into the base of a liquid water cloud by weak updrafts, e.g., in the case of fair weather cumuli (Siebert and Shaw, 2017). According to the discussion in Sect. 3.2 the overall uncertainty in the regression analysis of $n_{100,\mathrm{d}}$ with σ_{d} is of the order of a factor of 2–3. In Fig. 9, an uncertainty factor of 2 is considered by the dashed lines. Compared to this factor-2 uncertainty margin, the impact of uncertainties introduced by the applied conversion parameters is small.

Figure 10 shows the POLIPHON results in terms of ice-nucleating particle concentrations. As outlined in detail in Mamouri and Ansmann (2016), the POLIPHON data analysis delivers height profiles of the large-particle number concentration $n_{250,\mathrm{d}}$ and of the dust surface area concentration s_{d} in Fig. 10a with an accuracy of about 25-30% in the case of pronounced dust layers. Again, we applied two contrasting conversion parameter sets (Dushanbe, Cabo Verde). The differences in the results are well covered by the overall POLIPHON uncertainties of 30%.

The profile of $n_{250,\mathrm{d}}$ is then input in the INPC computation (see Fig. 10b, D15 parameterization) (DeMott et al., 2015) and the profile of s_{d} is needed as input in the INPC parameterization of Ullrich et al. (2017) (denoted as U17-D in Fig. 10b). Besides the aerosol profiles, actual temperature profiles are required in the calculations of $n_{\mathrm{INP,d}}$ profiles. D15 allows us to estimate INPC for immersion freezing which describes freezing of liquid droplets in which ice-nucleating particles are immersed. U17-D delivers INPC for deposition freezing. This ice nucleation mode describes direct water vapor deposition and freezing on favorable ice-nucleating particles. Deposition freezing usually takes place in the upper troposphere at temperatures clearly below -30°C and depends on the ice supersaturation level S_{ICE} in an ascending air parcel. Thus, S_{ICE} is also an input parameter and typically set to 1.15 as in Fig. 10b. It it noteworthy to mention that a decrease of temperature by 5 K increases INPC by an order of magnitude.

According to the extended uncertainty analysis and field observations (see the recent discussions in Marinou et al. (2018) and Ansmann et al. (2019)) an overall uncertainty in the INPC estimation of an order of magnitude (factor of 3) has always to be taken into account in the data interpretation. This is indicated as dashed lines in Fig. 10b. As can be seen, compared to this uncertainty the impact of the use of different conversion factors in the retrieval of $n_{250,\mathrm{d}}$ and s_{d} is of minor importance in the uncertainty discussion.

In Fig. 10b, we added an INPC profile segment (from 8.5–10 km) based on observations in cloud free air from 15:15-16:10 UTC (see Fig. 6, just before the time period indicated by the white frame) to extend the INPC profile up to the height

range where several cirrus layers formed. The patchy ice cloud cluster at 7 km between 15:00 and 16:30 UTC (see Fig. 6) probably formed via immersion freezing at temperatures around −25°C. INPC was high with 1-10 L^{-1}, and thus triggered the nucleation of 1-10 ice crystals per liter. Higher up, at 9-11 km and corresponding temperatures from −35 to −50°C, deposition freezing prevails besides homogeneous freezing. The use of the U17-D parameterization indicates INPC values of 0.1-1 L^{-1} which is relatively low and may explain the short-lived thin ice cloud features (occurring after 16:15 UTC) and the absence of large cirrus fields with extended virga zones.

5 Conclusions

An extended global AERONET analysis has been performed to create a global data sets of dust-related POLIPHON conversion factors. We analyzed AERONET observations for all relevant desert regions in Africa, Middle East, Central and East Asia, America, and Australia and provide respective regional conversion parameter sets. Significant differences in the obtained conversion parameters caused by potentially different dust composition and size distribution characteristics for different desert regions were not found. Furthermore, the presented Tajikistan case study showed that the use of different, contrasting conversion parameters did not have large impact on the overall uncertainty in the POLIPHON results.

Thus, it is justified to apply a global mean conversion parameter data set (as provided in Table 3) to analyse global dust aerosol observations. This is especially of advantage for spaceborne lidar applications. However, it is also recommended to use the regional conversion parameters derived for the 21 AERONET sites and for four continents in respective regional ground-based lidar studies of atmospheric dust, as performed in the Dushanbe case study.

In conclusion, we can state that appropriate conversion parameters are now available for mineral dust around the globe. In addition, conversion parameters representing pure marine conditions are available from marine Barbados AERONET observations (Mamouri and Ansmann, 2016, 2017). As an outlook, it remains to investigate in detail the conversion parameters for anthropogenic aerosol particles (urban haze, rural background aerosol, forest fire smoke, and free tropospheric smoke and haze by using mountain stations). A detailed study for anthropogenic aerosol conversion parameters has only be done so far for the urban, highly polluted AERONET stations of Leipzig and Limassol.

6 Data availability

All data used in this work can be accessed through the AERONET home page at https://aeronet.gsfc.nasa.gov/ (last access: 22 Februray 2019). Polly lidar observations (level 0 data, measured signals) are in the PollyNET data base (http://polly.rsd.tropos.de/). All the analysis products are available at TROPOS upon request (info@tropos.de).

7 Author contributions

AA and REM worked on the applied methodology and prepared the manuscript. JH provided the Dushanbe case study results. DA, JH, and SFA took care of the excellent performance of the Polly lidar and AERONET photometer during the 18-month CADEX field campaign.

8 Competing interests

The authors declare that they have no conflict of interest.

Acknowledgements. We are grateful to all PIs of the AERONET sites used in this study for maintaining their instruments and providing their data to the community. We thank AERONET for their continuous efforts in providing high-quality measurements and products. The authors acknowledge funding from the Horizon 2020 research and innovation program ACTRIS-2 Integrating Activities (H2020-INFRAIA-2014-2015, grant agreement no. 654109). We thank AERONET-Europe for providing calibration service. AERONET-Europe is also part of the ACTRIS-2 project. The CADEX project was funded by the German Federal Ministry of Education and Research in the context of 'Partnerships for sustainable problem solving in emerging and developing countries' under the grant number 01DK14014. Aerosol sources apportionment analysis has been supported by air mass transport computation with the NOAA (National Oceanic and Atmospheric Administration) HYSPLIT (HYbrid Single-Particle Lagrangian Integrated Trajectory) model using GDAS meteorological data.

References

AERONET: AERONET aerosol data base, available at: http://aeronet.gsfc.nasa.gov/, last access: 22 Februray, 2019.

Ansmann, A., Seifert, P., Tesche, M., and Wandinger, U.: Profiling of fine and coarse particle mass:case studies of Saharan dust and Eyjafjallajökull/Grimsvötn volcanic plumes, Atmos. Chem. Phys., 12, 9399-9415, doi:10.5194/acp-12-9399-2012, 2012.

Ansmann, A., Baars, H., Chudnovsky, A., Mattis, I., Veselovskii, I., Haarig, M., Seifert, P., Engelmann, R., and Wandinger, U.: Extreme levels of Canadian wildfire smoke in the stratosphere over central Europe on 21–22 August 2017, Atmos. Chem. Phys., 18, 11831-11845, https://doi.org/10.5194/acp-18-11831-2018, 2018.

Ansmann, A., Mamouri, R.-E., Bühl, J., Seifert, P., Engelmann, R., Hofer, J., Nisantzi, A., Atkinson, J., Kanji, Z., Amiridis, V., Vrekoussis, M., and Sciare, J.: Closure between ice-nucleating particle and ice crystal number concentration: Active remote sensing of altocumulus and cirrus clouds in Saharan dust over Cyprus, Atmos. Chem. Phys., in preparation, 2019.

Baars, H., Kanitz, T., Engelmann, R., Althausen, D., Heese, B., Komppula, M., Preißler, J., Tesche, M., Ansmann, A., Wandinger, U., Lim, J.-H., Ahn, J. Y., Stachlewska, I. S., Amiridis, V., Marinou, E., Seifert, P., Hofer, J., Skupin, A., Schneider, F., Bohlmann, S., Foth, A., Bley, S., Pfüller, A., Giannakaki, E., Lihavainen, H., Viisanen, Y., Hooda, R. K., Pereira, S. N., Bortoli, D., Wagner, F., Mattis, I., Janicka, L., Markowicz, K. M., Achtert, P., Artaxo, P., Pauliquevis, T., Souza, R. A. F., Sharma, V. P., van Zyl, P. G., Beukes, J. P., Sun, J., Rohwer, E. G., Deng, R., Mamouri, R.-E., and Zamorano, F.: An overview of the first decade of PollyNET: an emerging network of automated Raman-polarization lidars for continuous aerosol profiling, Atmos. Chem. Phys., 16, 5111-5137, https://doi.org/10.5194/acp-16-5111-2016, 2016.

Bohlmann, S., Baars, H., Radenz, M., Engelmann, R., and Macke, A.: Ship-borne aerosol profiling with lidar over the Atlantic Ocean: from pure marine conditions to complex dust–smoke mixtures, Atmos. Chem. Phys., 18, 9661-9679, https://doi.org/10.5194/acp-18-9661-2018, 2018.

Cordoba-Jabonero, C., Sicard, M., Ansmann, A., del Aguila, A., and Baars, H.: Separation of the optical and mass features of particle components in different aerosol mixtures by using POLIPHON retrievals in synergy with continuous polarized Micro-Pulse Lidar (P-MPL) measurements, Atmos. Meas. Tech., 11, 4775-4795, https://doi.org/10.5194/amt-11-4775-2018, 2018.

DeMott, P. J., Prenni, A. J., Liu, X., Kreidenweis, S. M., Petters, M. D., Twohy, C. H., Richardson, M. S., Eidhammer, T., and Rogers, D. C.: Predicting global atmospheric ice nuclei distributions and their impacts on climate, Proc. Natl. Acad. Sci. USA, 107, 11217–11222, doi:10.1073/pnas.0910818107, 2010.

DeMott, P. J., Prenni, A. J., McMeeking, G. R., Sullivan, R. C., Petters, M. D., Tobo, Y., Niemand, M., Möhler, O., Snider, J. R., Wang, Z., and Kreidenweis, S. M.: Integrating laboratory and field data to quantify the immersion freezing ice nucleation activity of mineral dust particles, Atmos. Chem. Phys., 15, 393–409, doi:10.5194/acp-15-393-2015, 2015.

Düsing, S., Wehner, B., Seifert, P., Ansmann, A., Baars, H., Ditas, F., Henning, S., Ma, N., Poulain, L., Siebert, H., Wiedensohler, A., and Macke, A.: Helicopter-borne observations of the continental background aerosol in combination with remote sensing and ground-based measurements, Atmos. Chem. Phys., 18, 1263-1290, https://doi.org/10.5194/acp-18-1263-2018, 2018.

Engelmann, R., Kanitz, T., Baars, H., Heese, B., Althausen, D., Skupin, A., Wandinger, U., Komppula, M., Stachlewska, I. S., Amiridis, V., Marinou, E., Mattis, I., Linné, H., and Ansmann, A.: The automated multiwavelength Raman polarization and water-vapor lidar PollyXT: the neXT generation, Atmos. Meas. Tech., 9, 1767-1784, doi:10.5194/amt-9-1767-2016, 2016.

Freudenthaler, V., Esselborn, M., Wiegner, M., Heese, B., Tesche, M., Ansmann, A., Müller, D., Althausen, D., Wirth, M., Fix, A., Ehret, G., Knippertz, P., Toledano, C., Gasteiger, J., Garhammer, M., and Seefeldner, M.: Depolarization ratio profiling at several wavelengths in pure Saharan dust during SAMUM 2006, Tellus B, 61, 165-179, doi: 10.1111/j.1600-0889.2008.00396.x, 2009.

GDAS: Global Data Assimilation System, meteorological data base, available at: https://www.ready.noaa.gov/gdas05.php, last access: 20 February, 2019.

Giles, D. M., Sinyuk, A., Sorokin, M. G., Schafer, J. S., Smirnov, A., Slutsker, I., Eck, T. F., Holben, B. N., Lewis, J. R., Campbell, J. R., Welton, E. J., Korkin, S. V., and Lyapustin, A. I.: Advancements in the Aerosol Robotic Network (AERONET) Version 3 database – automated near-real-time quality control algorithm with improved cloud screening for Sun photometer aerosol optical depth (AOD) measurements, Atmos. Meas. Tech., 12, 169-209, https://doi.org/10.5194/amt-12-169-2019, 2019.

Haarig, M., Ansmann, A., Baars, H., Jimenez, C., Veselovskii, I., Engelmann, R., and Althausen, D.: Depolarization and lidar ratios at 355, 532, and 1064 nm and microphysical properties of aged tropospheric and stratospheric Canadian wildfire smoke, Atmos. Chem. Phys., 18, 11847-11861, https://doi.org/10.5194/acp-18-11847-2018, 2018.

Holben, B. N., Eck, T. F., Slutsker, I., Tanré, D., Buis, J. P., Setzer, A., Vermote, E., Reagan, J. A., Kaufman, Y. J., Nakajima, T., Lavenu, F., Jankowiak, I., and Smirnov, A.: AERONET – a federated instrument network and data archive for aerosol characterization, Remote Sens. Environ., 66, 1–16, 1998.

Hofer, J., Althausen, D., Abdullaev, S. F., Makhmudov, A. N., Nazarov, B. I., Schettler, G., Engelmann, R., Baars, H., Fomba, K. W., Müller, K., Heinold, B., Kandler, K., and Ansmann, A.: Long-term profiling of mineral dust and pollution aerosol with multiwavelength polarization Raman lidar at the Central Asian site of Dushanbe, Tajikistan: case studies, Atmos. Chem. Phys., 17, 14559-14577, https://doi.org/10.5194/acp-17-14559-2017, 2017.

Hoose, C. and Möhler, O.: Heterogeneous ice nucleation on atmospheric aerosols: a review of results from laboratory experiments, Atmos. Chem. Phys., 12, 9817-9854, https://doi.org/10.5194/acp-12-9817-2012, 2012.

HYSPLIT: HYbrid Single-Particle Lagrangian Integrated Trajectory model, backward trajectory calculation tool, available at: http://ready.arl.noaa.gov/HYSPLIT_traj.php, last access: 22 February, 2019.

Illingworth, A. J., Barker, H. W., Beljaars, A., Ceccaldi, M., Chepfer, H., Clerbaux, N., Cole, J., Delanoe, J., Domenech, C., Donovan, D. P., Fukuda, S., Hirakata, M., Hogan, R. J., Huenerbein, H., Kollias, P., Kubota, T., Nakajima, T., Nakajima, T. Y., Nishizawa, T., Ohno, Y., Okamoto, H., Oki, R., Sato, K., Satoh, M., Shephard, M., Velázquez-Blázquez, A., Wandinger, U., Wehr, T., and Zadelhoff, G.-J.: The EARTHCARE satellite: the next step forward in global measurements of clouds, aerosols, precipitation and radiation, B. Am. Meteorol. Soc., 96, 1311–1332, doi:10.1175/BAMS-D-12-00227.1, 2015.

Kanji, Z. A., Ladino, L. A., Wex, H., Boose, Y., Burkert-Kohn, M., Cziczo, D. J., and Krämer, M.: Chapter 1: Overview of ice nucleating particles, Meteor Monogr., Am. Meteorol. Soc., 58, 1-33, https://doi.org/10.1175/amsmonographs-d-16-0006.1, 2017.

Kanitz, T., Ansmann, A., Engelmann, R., and Althausen, D.: North-south cross sections of the vertical aerosol distribution over the Atlantic Ocean from multiwavelength Raman/polarization lidar during Polarstern cruises, J. Geophys. Res. Atmos., 118, 2643–2655, doi:10.1002/jgrd.50273, 2013.

Lv, M., Wang, Z., Li, Z., Luo, T., Ferrare, R., Liu, D., Wu, D., Mao, J., Wan, B., Zhang, F., and Wang, Y.: Retrieval of cloud condensation nuclei number concentration profiles from lidar extinction and backscatter data, J. Geophys. Res. Atmos., 123, 6082-6098, https://doi.org/10.1029/2017JD028102, 2018.

Mamali, D., Marinou, E., Sciare, J., Pikridas, M., Kokkalis, P., Kottas, M., Binietoglou, I., Tsekeri, A., Keleshis, C., Engelmann, R., Baars, H., Ansmann, A., Amiridis, V., Russchenberg, H., and Biskos, G.: Vertical profiles of aerosol mass concentration derived by unmanned

airborne in situ and remote sensing instruments during dust events, Atmos. Meas. Tech., 11, 2897-2910, https://doi.org/10.5194/amt-11-2897-2018, 2018.

Mamouri, R. E. and Ansmann, A.: Fine and coarse dust separation with polarization lidar, Atmos. Meas. Tech., 7, 3717-3735, doi:10.5194/amt-7-3717-2014, 2014.

Mamouri, R. E. and Ansmann, A.: Estimated desert-dust ice nuclei profiles from polarization lidar: methodology and case studies, Atmos. Chem. Phys., 15, 3463-3477, doi:10.5194/acp-15-3463-2015, 2015.

Mamouri, R.-E. and Ansmann, A.: Potential of polarization lidar to provide profiles of CCN- and INP-relevant aerosol parameters, Atmos. Chem. Phys., 16, 5905-5931, doi:10.5194/acp-16-5905-2016, 2016.

Mamouri, R.-E. and Ansmann, A.: Potential of polarization/Raman lidar to separate fine dust, coarse dust, maritime, and anthropogenic aerosol profiles, Atmos. Meas. Tech., 10, 3403-3427, https://doi.org/10.5194/amt-10-3403-2017, 2017.

Marinou, E., Amiridis, V., Binietoglou, I., Tsikerdekis, A., Solomos, S., Proestakis, E., Konsta, D., Papagiannopoulos, N., Tsekeri, A., Vlastou, G., Zanis, P., Balis, D., Wandinger, U., and Ansmann, A.: Three-dimensional evolution of Saharan dust transport towards Europe based on a 9-year EARLINET-optimized CALIPSO dataset, Atmos. Chem. Phys., 17, 5893-5919, https://doi.org/10.5194/acp-17-5893-2017, 2017.

Marinou, E., Tesche, M., Nenes, A., Ansmann, A., Schrod, J., Mamali, D., Tsekeri, A., Pikridas, M., Baars, H., Engelmann, R., Voudouri, K.-A., Solomos, S., Sciare, J., Groß, S., and Amiridis, V.: Retrieval of ice nucleating particle concentrations from lidar observations: Comparison with airborne in-situ measurements from UAVs, Atmos. Chem. Phys. Disc., 16, https://doi.org/10.5194/acpd-2018-1203, 2018.

Murray, B. J., O'Sullivan, D., Atkinson, J. D., and Webb, M. E.: Ice nucleation by particles immersed in supercooled cloud droplets, Chem. Soc. Rev., 41, 6519–6554, https://doi.org/10.1039/c2cs35200a, 2012.

Niemand, M., Möhler, O., Vogel, B., Vogel, H., Hoose, C., Connolly, P., Klein, H., Bingemer, H., DeMott, P., Skrotzki, J., and Leisner, T.: Parameterization of immersion freezing on mineral dust particles: an application in a regional scale model, J. Atmos. Sci., 69, 3077–3092, 2012.

Rolph, G., Stein, A., and Stunder, B.: Real-time Environmental Applications and Display sYstem: READY. Environmental Modelling & Software, 95, 210-228, https://doi.org/10.1016/j.envsoft.2017.06.025, 2017.

Schrod, J., Weber, D., Drücke, J., Keleshis, C., Pikridas, M., Ebert, M., Cvetkovic, B., Nickovic, S., Marinou, E., Baars, H., Ansmann, A., Vrekoussis, M., Mihalopoulos, N., Sciare, J., Curtius, J., and Bingemer, H. G.: Ice nucleating particles over the Eastern Mediterranean measured by unmanned aircraft systems, Atmos. Chem. Phys., 17, 4817-4835, https://doi.org/10.5194/acp-17-4817-2017, 2017.

Shinozuka, Y., Clarke, A. D., Nenes, A., Jefferson, A., Wood, R., McNaughton, C. S., Ström, J., Tunved, P., Redemann, J., Thornhill, K. L., Moore, R. H., Lathem, T. L., Lin, J. J., and Yoon, Y. J.: The relationship between cloud condensation nuclei (CCN) concentration and light extinction of dried particles: indications of underlying aerosol processes and implications for satellite-based CCN estimates, Atmos. Chem. Phys., 15, 7585-7604, doi:10.5194/acp-15-7585-2015, 2015.

Shupe, M. D.: A ground–based multisensor cloud phase classifier, Geophys. Res. Letts., 34, L22809, doi:10.1029/2007GL031008.

Siebert, H. and Shaw, R.: Supersaturation Fluctuations during the Early Stage of Cumulus Formation, J. Atmos. Sci., 74, 975-988, https://doi.org/10.1175/JAS-D-16-0115.1, 2017.

Stein, A.F., Draxler, R.R, Rolph, G.D., Stunder, B.J.B., Cohen, M.D., and Ngan, F.: NOAA's HYSPLIT atmospheric transport and dispersion modeling system, Bull. Amer. Meteor. Soc., 96, 2059-2077, http://dx.doi.org/10.1175/BAMS-D-14-00110.1, 2015

Tesche, M., Müller, D., Groß, S., Ansmann, A., Althausen, D., Freudenthaler, V., Weinzierl, B., Veira, A., and Petzold, A.: Optical and microphysical properties of smoke over Cape Verde inferred from multiwavelength lidar measurements. Tellus B, 63, 677–694, doi:10.1111/j.1600-0889.2011.00549.x, 2011.

Ullrich, R., Hoose, C., Möhler, O., Niemand, M., Wagner, R., Höhler, K., Hiranuma, N., Saathoff, H., and Leisner, T.: A new ice nucleation active site parameterization for desert dust and soot, J. Atmos. Sci., 74, 699–717, 2017.

Winker, D. M., Vaughan, M. A., Omar, A., Hu, Y., Powell, K. A., Liu, Z., Hunt, W. H., and Young, S. A.: Overview of the CALIPSO mission and CALIOP data processing algorithms, J. Atmos. Oceanic Technol., 26, 2310-2323, 2009.

Atmos. Meas. Tech. Discuss., https://doi.org/10.5194/amt-2019-98
Manuscript under review for journal Atmos. Meas. Tech.
Discussion started: 14 March 2019

Atmospheric Measurement Techniques Discussions

Table 1. Overview of the dust-related conversions within the POLIPHON data analysis. Mass concentrations M_{d}, M_{df}, and M_{dc} are obtained from measured dust extinction coefficients σ_{d}, σ_{df}, and σ_{dc} by means of volume conversion factors $c_{\mathrm{v,d}}$, $c_{\mathrm{v,df}}$, and $c_{\mathrm{v,dc}}$ and assuming a dust particle density ρ_{d} of 2.6 $\mathrm{g/cm^{-3}}$. Conversion of σ_{d} into number concentrations $n_{100,\mathrm{d}}$ and $n_{250,\mathrm{d}}$, and surface area concentration s_{d} by means of the respective conversion parameters $c_{100,\mathrm{d}}$, $c_{250,\mathrm{d}}$, $c_{\mathrm{s,d}}$, and exponent x_{d} are needed to provide the input in the estimation of CCN concentration $n_{\mathrm{CCN,d}}$ and INP concentration $n_{\mathrm{INP,d}}$. The input parameter $f_{ss,\mathrm{d}}$ is 1.0 in the CCN estimation for a water supersaturation value of 0.2% and > 1.0 for supersaturations of 0.25% and higher. D15 (DeMott et al., 2015), U17-I (immersion freezing), and U17-D (deposition freezing) (Ullrich et al., 2017) are the applied INP parameterization schemes. Besides the aerosol profiles, the temperature profile $T(z)$ is required in the $n_{\mathrm{INP,d}}$ estimation. The ice supersaturation S_{ice} needed in the U17-D computation may be set to a typical values of 1.15. See the text in Sect. 2 for more details.

Parameter	**Equation/method (reference)**	**Input**
Dust mass concentration	$M_{\mathrm{d}}(z) = \rho_{\mathrm{d}} c_{\mathrm{v,d}} \sigma_{\mathrm{d}}(z)$	$\sigma_{\mathrm{d}}(z), \rho_{\mathrm{d}}$
Fine dust mass concentration	$M_{\mathrm{df}}(z) = \rho_{\mathrm{d}} c_{\mathrm{v,df}} \sigma_{\mathrm{df}}(z)$	$\sigma_{\mathrm{df}}(z), \rho_{\mathrm{d}}$
Coarse dust mass concentration	$M_{\mathrm{dc}}(z) = \rho_{\mathrm{d}} c_{\mathrm{v,dc}} \sigma_{\mathrm{dc}}(z)$	$\sigma_{\mathrm{dc}}(z), \rho_{\mathrm{d}}$
Dust particle number conc. (radius>100 nm)	$n_{100,\mathrm{d}}(z) = c_{100,\mathrm{d}} \times \sigma_{\mathrm{d}}^{x_{\mathrm{d}}}(z)$	$\sigma_{\mathrm{d}}(z)$
Dust particle number conc. (radius>250 nm)	$n_{250,\mathrm{d}}(z) = c_{250,\mathrm{d}} \times \sigma_{\mathrm{d}}(z)$	$\sigma_{\mathrm{d}}(z)$
Dust particle surface area conc.	$s_{\mathrm{d}}(z) = c_{\mathrm{s,d}} \times \sigma_{\mathrm{d}}(z)$	$\sigma_{\mathrm{d}}(z)$
Dust-related CCN concentration	$n_{\mathrm{CCN},ss,\mathrm{d}}(z) = f_{ss,\mathrm{d}} \times n_{100,\mathrm{d}}(z)$	$n_{100,\mathrm{d}}(z), f_{ss,\mathrm{d}}$
Dust-related INP concentration	$n_{\mathrm{INP,d}}(z)$ (e.g., D15)	$n_{250,\mathrm{d}}(z), T(z)$
Dust-related INP concentration	$n_{\mathrm{INP,d}}(z)$ (e.g., U17-I)	$s_{\mathrm{d}}(z), T(z)$
Dust-related INP concentration	$n_{\mathrm{INP,d}}(z)$ (e.g., U17-D)	$s_{\mathrm{d}}(z), T(z), S_{\mathrm{ice}}$

Atmos. Meas. Tech. Discuss., https://doi.org/10.5194/amt-2019-98
Manuscript under review for journal Atmos. Meas. Tech.
Discussion started: 14 March 2019

Atmospheric Measurement Techniques Discussions

Table 2. Overview of AERONET stations considered in our study, selected observational periods for which version-3 level-2.0 data are available (Giles et al., 2019), total number of observations (inversion products), dust-related inversion cases (AE<0.3, AOT>0.1), and 532 nm AOT (mean and STD) for the dust observations only.

AERONET site	Acronym	Latitude, longitude	Time period, level-2.0 data	Obs.	Dust obs.	AOT
Tamanrasset, Algeria	TA	22.8°N, 5.5°E	30 Sep 2006 – 19 Jun 2018	7442	3542	0.37±0.28
Izana, Tenerife, Spain	IZ	28.3°N, 16.5°W	1 Nov 2004 –22 May 2018	3264	499	0.26±0.14
Sal, Cabo Verde	CV	16.7°N, 22.9°W	2 Nov 1994 – 9 Jun 2017	4718	2982	0.45±0.28
Dakar, Senegal	DK	14.4°N, 17.0°W	24 Jun 2000 – 12 Feb 2018	7985	3823	0.60±0.33
Banizoumbou, Niger	BA	13.5°N, 2.7°E	17 Oct 1995 – 15 Mar 2017	8547	3875	0.65±0.39
Ilorin, Nigeria	IL	8.5°N, 4.7°E	25 Apr 1998 – 26 Mar 2018	4024	466	1.20±0.59
Limassol, Cyprus	LI	34.7°N, 33.0°E	14 Apr 2010 - 5 May 2017	2606	72	0.43±0.22
Eilat, Israel	EI	26.5°N, 34.9°E	26 Nov 2007–22 June 2018	7213	657	0.39±0.26
Sede Boker, Israel	SB	30.9°N, 34.8°E	16 Oct 1995 – 14 Jan 2018	17005	1610	0.35±0.23
Nes Ziona, Israel	NZ	31.9°N, 34.8°E	17 Dec 2000 – 14 Nov 2015	5268	410	0.48±0.32
Solar Village, Saudi Arabia	SV	24.9°N, 46.4°E	23 Feb 1999 – 15 Dec 2012	14284	4199	0.51±0.30
Mezaira, United Arab Emirates	ME	23.1°N, 53.8°E	8 Jun 2004 – 8 May 2018	7354	1055	0.55±0.28
Dushanbe, Tajikistan	DU	38.6°N, 68.9°E	5 Jul 2010– 11 Apr 2018	3808	325	0.65±0.40
Lanzhou(SACOL), China	LA	35.9°N, 104.1°E	28 Jun 2006 – 3 May 2013	3384	218	0.68±0.37
Dalanzadgad, Mongolia	DA	43.6°N, 104.4°E	27 Mar 1998 – 25 Dec 2017	2577	49	0.29±0.16
Tuscon, Arizona, USA	TU	32.2°N, 111.0°W	24 Nov 1993 – 18 Apr 2018	4881	17	0.15±0.04
White-Sands, New Mexico, USA	WS	32.6°N, 106.3°W	17 Nov 2006 – 23 Jun 2018	6696	27	0.22±0.12
Trelew, Argentina	TR	43.2°S, 65.3°W	11 Nov 2005 – 12 Oct 2017	2770	21	0.16±0.05
Gobabeb, Namibia	GO	23.6°S, 15.0°E	11 Nov 2014 – 29 Jul 2018	5117	89	0.15±0.05
Birdsville, Australia	BI	25.9°S, 139.3°E	13 Aug 2005 – 17 Dec 2017	6578	59	0.25±0.12
Leipzig, Germany	LE	51.4°N, 12.4°E	20 May 2001 – 17 Oct 2017	2169	14	0.48±0.18

Atmos. Meas. Tech. Discuss., https://doi.org/10.5194/amt-2019-98
Manuscript under review for journal Atmos. Meas. Tech.
Discussion started: 14 March 2019

Atmospheric Measurement Techniques Discussions

Table 3. Dust conversion parameters required in the conversion of particle extinction coefficients σ_{d} at 532 nm into particle number, surface area and volume concentration (index d for total dust, index df for fine dust, index dc for coarse dust) as described in Table 1. The mean values and SD for $c_{\mathrm{v,d}}$, $c_{\mathrm{v,df}}$, and $c_{\mathrm{v,dc}}$ (in 10^{-12} Mm), of $c_{250,\mathrm{d}}$ (in Mm cm^{-3}), and $c_{\mathrm{s,d}}$ (in 10^{-12} Mm m^2 cm^{-3}) are derived from the extended AERONET data analysis described in Sects. 2 and 3.1 for all sites listed in Table 2. $c_{100,\mathrm{d}}$ (in cm^{-3} for $\sigma_d = 1$ Mm^{-1}), and x_d and respective standard deviations (SD) are obtained in the way described in Sect. 3.2 by considering only AOT from 0.1-0.6, except for Ilorin (all AOT are used because only 12% of AOT<0.6). No data ($c_{100,\mathrm{d}}$, x_d) are listed when the regression coefficient <0.6. The regional/continental mean values (for Africa, Middle East, Asia, America/Australia) are obtained by observation-weighted averaging of the given station mean and SD values. The Africa/Asia mean values (estimates, last line) may be used as global mean parameters in spaceborne applications.

AERONET site	$c_{\mathrm{v,d}}$	$c_{\mathrm{v,df}}$	$c_{\mathrm{v,dc}}$	$c_{250,\mathrm{d}}$	$c_{\mathrm{s,d}}$	$c_{100,\mathrm{d}}$	x_{d}
Tamanrasset, Algeria	0.67 ± 0.07	0.24 ± 0.02	0.81 ± 0.08	0.18 ± 0.03	2.52 ± 0.60	5.80 ± 0.42	0.79 ± 0.01
Izana, Teneriffe	0.59 ± 0.05	0.22 ± 0.05	0.72 ± 0.06	0.20 ± 0.02	2.39 ± 0.52	6.85 ± 1.07	0.73 ± 0.03
Sal, Cabo Verde	0.64 ± 0.07	0.22 ± 0.06	0.79 ± 0.08	0.20 ± 0.03	2.24 ± 0.55	1.24 ± 0.13	1.04 ± 0.02
Dakar, Senegal	0.69 ± 0.08	0.23 ± 0.07	0.84 ± 0.09	0.18 ± 0.03	2.54 ± 0.62	7.42 ± 0.81	0.78 ± 0.02
Banizoumbou, Niger	0.72 ± 0.09	0.24 ± 0.07	0.89 ± 0.11	0.18 ± 0.03	2.49 ± 0.63	6.69 ± 0.60	0.80 ± 0.02
Ilorin, Nigeria	0.73 ± 0.11	0.28 ± 0.08	0.91 ± 0.15	0.18 ± 0.03	3.04 ± 0.90	4.52 ± 1.15	0.88 ± 0.04
North Africa mean	0.68 ± 0.08	0.23 ± 0.06	0.83 ± 0.09	0.18 ± 0.03	2.47 ± 0.61	5.53 ± 0.55	0.84 ± 0.02
Eilat, Israel	0.67 ± 0.09	0.21 ± 0.05	0.83 ± 0.10	0.16 ± 0.03	2.40 ± 0.51	10.74 ± 2.11	0.70 ± 0.03
Sede Boker, Israel	0.66 ± 0.09	0.23 ± 0.06	0.81 ± 0.11	0.18 ± 0.03	2.54 ± 0.61	8.32 ± 0.92	0.73 ± 0.02
Nes Ziona, Israel	0.65 ± 0.08	0.24 ± 0.08	0.80 ± 0.09	0.18 ± 0.03	2.76 ± 0.95	7.84 ± 2.20	0.75 ± 0.05
Solar Village, Saudi Arabia	0.74 ± 0.08	0.24 ± 0.07	0.90 ± 0.10	0.15 ± 0.02	2.66 ± 0.69	11.98 ± 1.06	0.69 ± 0.02
Mezaira, UAE	0.69 ± 0.08	0.24 ± 0.06	0.85 ± 0.11	0.16 ± 0.02	2.77 ± 0.62	4.27 ± 0.65	0.89 ± 0.03
Middle East mean	0.71 ± 0.08	0.24 ± 0.07	0.86 ± 0.10	0.16 ± 0.02	2.63 ± 0.66	9.89 ± 1.12	0.73 ± 0.02
Dushanbe, Tajikistan	0.79 ± 0.09	0.27 ± 0.08	0.96 ± 0.12	0.13 ± 0.03	3.11 ± 0.87	12.36 ± 3.49	0.71 ± 0.05
Lanzhou, China	0.77 ± 0.09	0.27 ± 0.09	0.94 ± 0.11	0.15 ± 0.02	3.10 ± 0.94	12.20 ± 4.70	0.70 ± 0.06
Dalanzadgad, Mongolia	0.73 ± 0.17	0.21 ± 0.05	0.92 ± 0.19	0.15 ± 0.04	2.45 ± 0.48	–	–
Asia mean	0.78 ± 0.10	0.27 ± 0.08	0.95 ± 0.12	0.14 ± 0.03	3.05 ± 0.86	12.29 ± 3.97	0.71 ± 0.05
Tuscon, USA	0.79 ± 0.15	0.22 ± 0.04	0.98 ± 0.17	0.13 ± 0.03	2.36 ± 0.22	4.57 ± 5.10	0.88 ± 019
White-Sands, USA	0.94 ± 0.12	0.22 ± 0.05	1.11 ± 0.12	0.10 ± 0.03	2.25 ± 0.24	–	–
Trelew, Argentina	0.89 ± 0.12	0.22 ± 0.07	1.08 ± 0.14	0.13 ± 0.03	2.47 ± 0.73	–	–
Birdsville, Australia	0.90 ± 0.13	0.25 ± 0.07	1.07 ± 0.15	0.11 ± 0.03	2.43 ± 0.46	8.62 ± 5.90	0.69 ± 0.12
America/Australia mean	0.89 ± 0.13	0.23 ± 0.06	1.07 ± 0.14	0.11 ± 0.03	2.39 ± 0.42	7.71 ± 5.72	0.73 ± 0.13
Gobabeb, Namibia	0.62 ± 0.08	0.20 ± 0.04	0.81 ± 0.09	0.21 ± 0.05	2.25 ± 0.46	–	–
Limassol, Cyprus	0.64 ± 0.08	0.27 ± 0.08	0.79 ± 0.09	0.18 ± 0.03	3.07 ± 0.86	–	–
Leipzig, Germany	0.65 ± 0.10	0.26 ± 0.09	0.79 ± 0.11	0.20 ± 0.04	2.93 ± 1.02	–	–
Africa/Asia mean	0.71 ± 0.07	0.24 ± 0.06	0.86 ± 0.09	0.17 ± 0.03	2.7 ± 0.70	6.0 ± 0.6	0.80 ± 0.02

Atmos. Meas. Tech. Discuss., https://doi.org/10.5194/amt-2019-98
Manuscript under review for journal Atmos. Meas. Tech.
Discussion started: 14 March 2019

Atmospheric Measurement Techniques Discussions

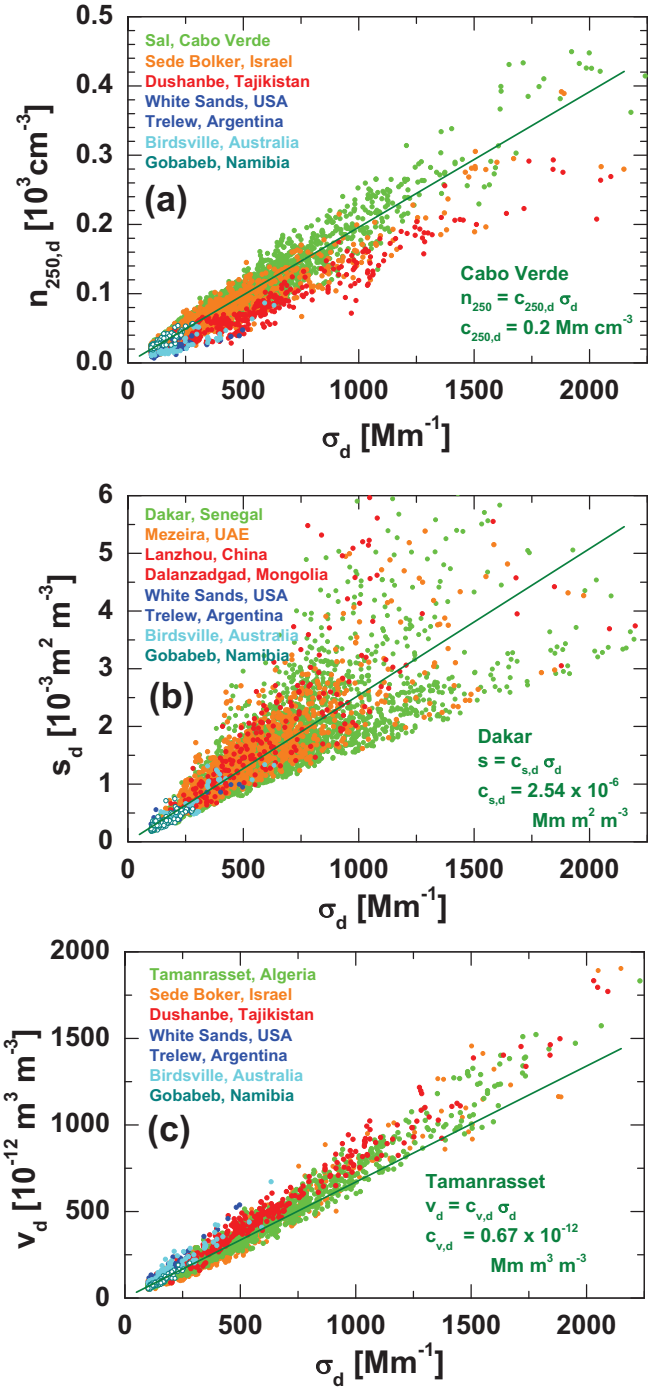

Figure 1. Relationship between dust extinction coefficient σ_d (532 nm) and (a) dust particle number concentration $n_{250,d}$, (b) surface area concentration s_d, and (c) volume concentration v_d. Correlations are shown for dust-dominated AERONET data sets (AE< 0.3 and AOT>0.1 or σ_d >100 Mm^{-1}) collected at sites in or close to major desert regions around the globe (indicated by different colors: green, northern Africa, orange, Middle East, red, Asia, blue, America, cyan, Australia, blue-green, southern Africa). The slopes of the dark green lines indicate the mean increase of $n_{250,d}$, s_d, and v_d with σ_d for the African stations as defined in Sect. 2 (Eqs. 6, 9, 10) and thus the conversion factors $c_{250,d}$ (a), $c_{s,d}$ (b), and $c_{v,d}$ (c), also given as numbers in (a), (b), and (c). All conversion parameters obtained from the entire AERONET analysis are listed in Table 3.

Atmos. Meas. Tech. Discuss., https://doi.org/10.5194/amt-2019-98
Manuscript under review for journal Atmos. Meas. Tech.
Discussion started: 14 March 2019

Atmospheric Measurement Techniques Discussions

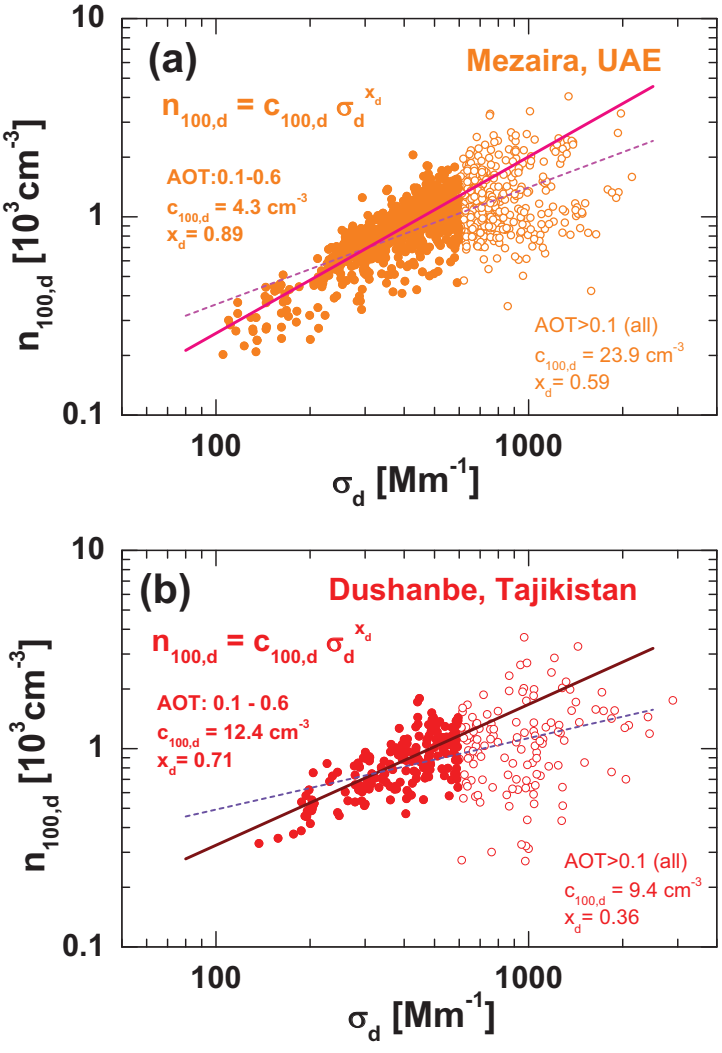

Figure 2. Relationship between dust extinction coefficient σ_{d} (532 nm) and dust particle number concentration $n_{100,\mathrm{d}}$ for AERONET dust observations at (a) Mezaira and (b) Dushanbe. Closed circles show the observations considering only 532 nm AOT values from 0.1-0.6. The open circles show all available observations (up to AOT of 3.0 or σ_{d}=3000 Mm^{-1}). The regression analysis is applied to the $\log(n_{100,\mathrm{d}})$-$\log(\sigma_{\mathrm{d}})$ data field for each of the four data sets. The results of the analysis are given as numbers in the figures. The straight lines indicate the mean increase of $\log(n_{100,\mathrm{d}})$ with $\log(\sigma_{\mathrm{d}})$ and thus the σ_{d} exponent x_{d}.

Atmos. Meas. Tech. Discuss., https://doi.org/10.5194/amt-2019-98
Manuscript under review for journal Atmos. Meas. Tech.
Discussion started: 14 March 2019

Atmospheric Measurement Techniques Discussions

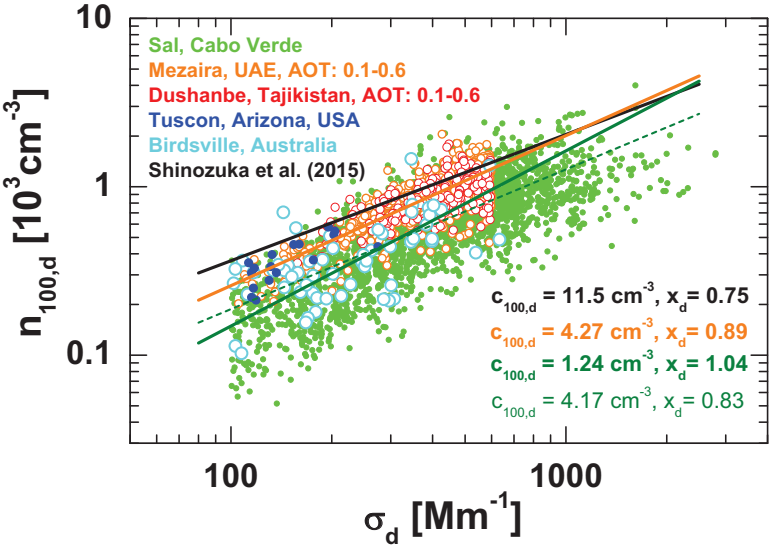

Figure 3. Relationship between dust extinction coefficient σ_d (532 nm) and dust particle number concentration $n_{100,d}$ for different dust-dominated AERONET data sets collected at the indicated stations. The given regression analysis results and straight lines are based on observations at Mezaira (open orange circles, orange line, AOT from 0.1-0.6) and Cabo Verde (green closed circles, dark dashed green line, AOT from 0.1-3.0, and dark green thick solid line, AOT from 0.1-0.6). The dust conversion parameters presented by Shinozuka et al. (2015) are shown for comparison (black line and black $c_{100,d}$ and x_d values).

Atmos. Meas. Tech. Discuss., https://doi.org/10.5194/amt-2019-98
Manuscript under review for journal Atmos. Meas. Tech.
Discussion started: 14 March 2019

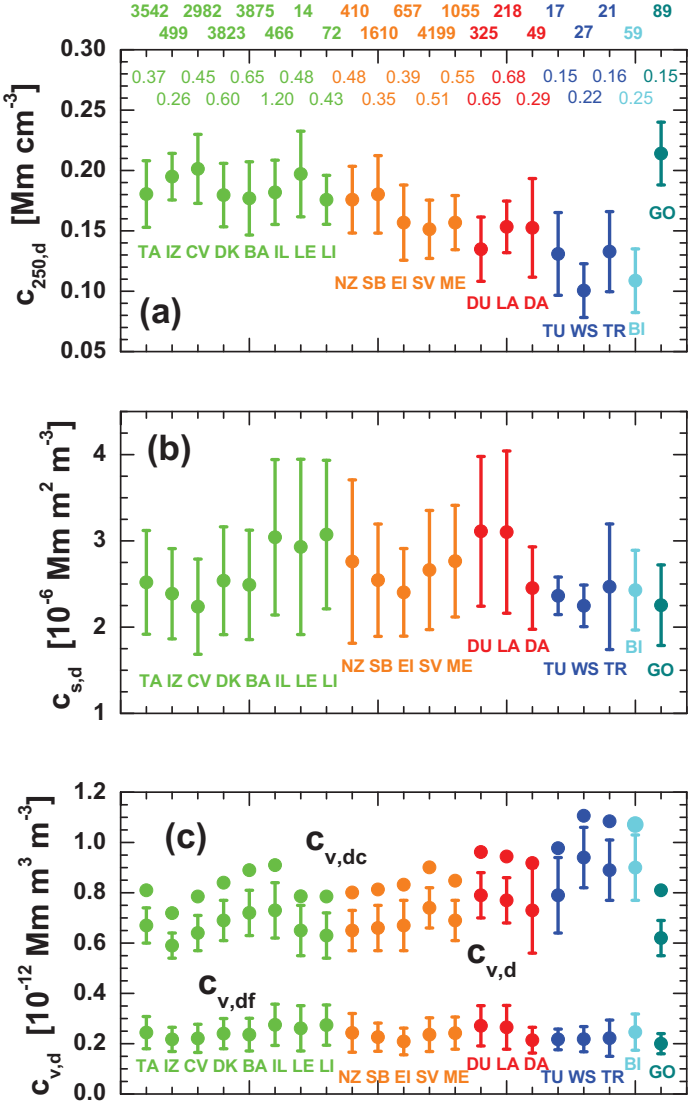

Figure 4. Overview of POLIPHON conversion factors (a) $c_{250,\mathrm{d}}$, (b) $c_{\mathrm{s,d}}$, and (c) $c_{\mathrm{v,d}}$ (mean and SD) derived from AERONET dust data sets collected at 21 stations around the world. The stations (and acronmys) are given in Table 2. Total numbers of observations (considered in the statistical analyses for each stations) are given above the figure frame (a) followed by two lines with respective mean 532 nm dust AOTs for all data sets (considering only the dust cases with AOT>0.1). All statistical results are also summarized in Table 3. In (c), volume-related conversion factors are separately determined for total (index d), fine (index df), and coarse dust (index dc). The uncertainty bars for $c_{\mathrm{v,dc}}$ are not shown, but similar to the ones for $c_{\mathrm{v,d}}$.

Atmos. Meas. Tech. Discuss., https://doi.org/10.5194/amt-2019-98
Manuscript under review for journal Atmos. Meas. Tech.
Discussion started: 14 March 2019

Atmospheric Measurement Techniques Discussions

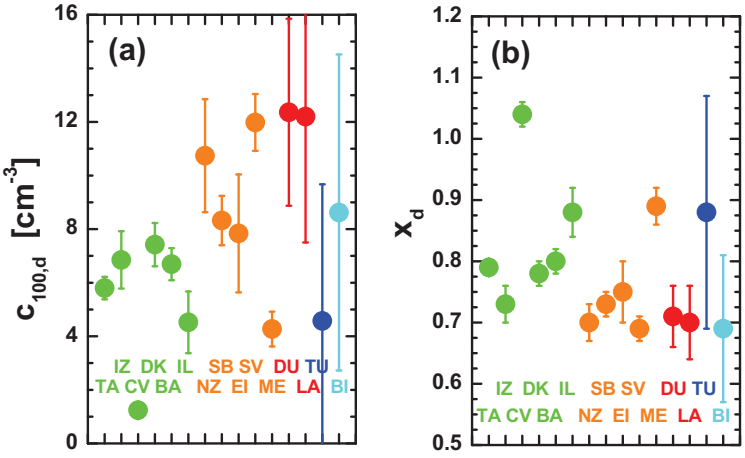

Figure 5. POLIPHON conversion parameters (a) $c_{100,\mathrm{d}}$ and (b) x_{d} derived from AERONET dust observations at 15 stations in northern Africa (green), the Middle East (orange), Central/East Asia (red), North America (blue), and Australia (light blue).

Atmos. Meas. Tech. Discuss., https://doi.org/10.5194/amt-2019-98
Manuscript under review for journal Atmos. Meas. Tech.
Discussion started: 14 March 2019

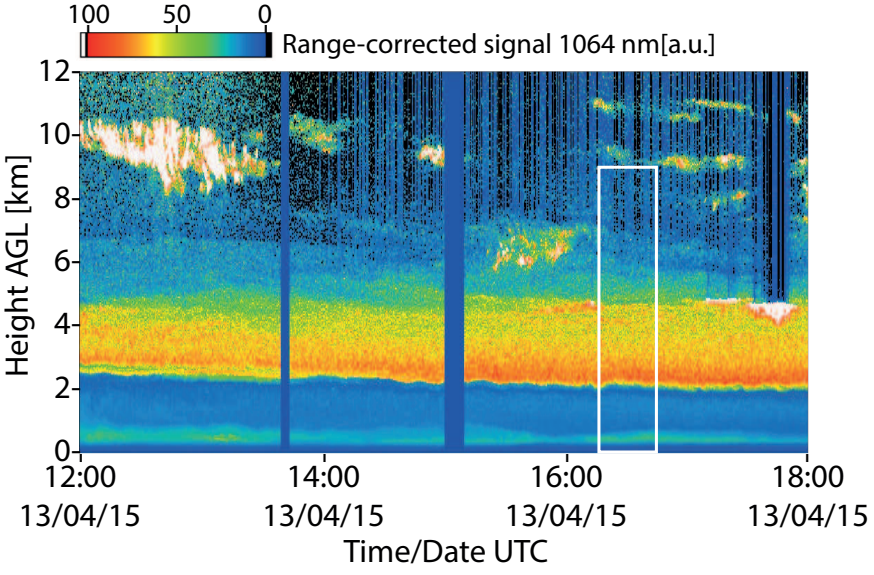

Figure 6. Dust layering over the central Asian AERONET site of Dushanbe, Tajikistan on 13 April 2015, observed with Polly lidar at 1064 nm (range-corrected signal). The densest layer from 2-5 km height AGL (above ground level) contained dust particles from Iran, Afganistan, and Oman according to the backward trajectories in Fig. 7. With increasing height, dust was advected from the Arabian peninsula and the Sahara. The polluted boundary layer reached up to about 2 km height and contained traces of local dust and dust from Kazakhstan. Above 6.5 km height (and temperatures $< -20°C$) ice clouds developed triggered by dust particles which are favorable ice-nucleating particles. POLIPHON results in Figs. 8-10 are derived for the height- and time range indicated by the white rectangle.

Atmos. Meas. Tech. Discuss., https://doi.org/10.5194/amt-2019-98
Manuscript under review for journal Atmos. Meas. Tech.
Discussion started: 14 March 2019

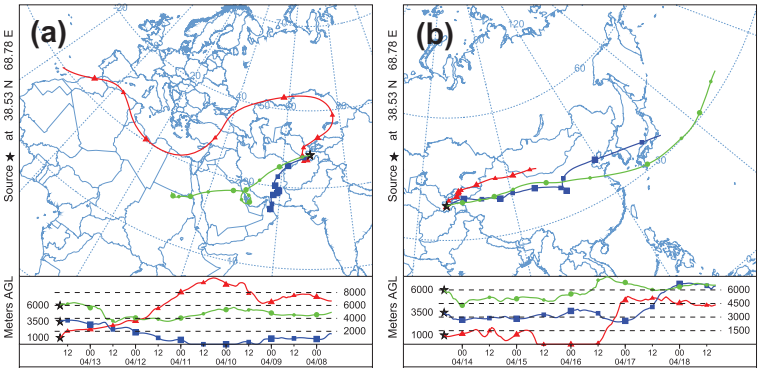

Figure 7. (a) Six-day backward trajectories and (b) six-day forward trajectories computed with the HYSPLIT (Hybrid Single Particle Lagrangian Integrated Trajectory) model (HYSPLIT, 2019; Stein et al., 2015; Rolph et al., 2017) for Dushanbe, Tajikistan, on 13 April 2015, 16:00 UTC. The computations are based on GDAS0.5 meteorological fields (GDAS, 2019). Arrival heights (a) and starting heights (b) are at 1000 m (red, in the boundary layer with Central Asian dust), 3500 m (blue, in a dense layer with dust from several western Asian deserts), and 6000 m (green, in dusty air from the Arabian peninsula and the Sahara).

Atmos. Meas. Tech. Discuss., https://doi.org/10.5194/amt-2019-98
Manuscript under review for journal Atmos. Meas. Tech.
Discussion started: 14 March 2019

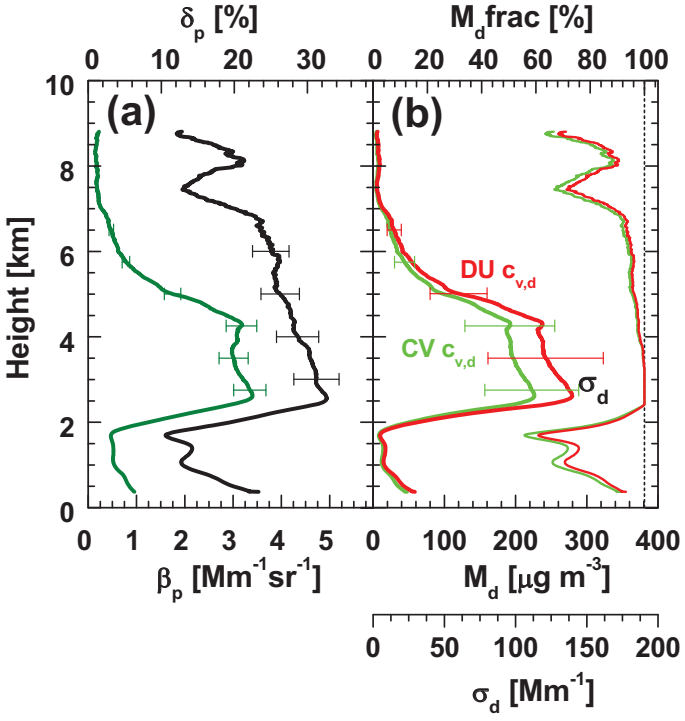

Figure 8. Retrieval of dust mass concentrations. From profiles of the particle backscatter coefficient β_{p} (green curve in (a), 532 nm) and particle linear depolarization ratio δ_{p} (black curve in (a), 532 nm) the profile of the dust extinction coefficient σ_{d} (red curve in b) is determined. The σ_{d} profile is converted into mass concentrations M_{d} (shown in (b) as thick lines) by means of volume conversion factors $c_{\mathrm{v,d}}$ of 0.64×10^{-12} Mm for Sal, Cabo Verde (CV, green M_{d} profile, see Table. 3) and 0.79×10^{-12} Mm for Dushanbe (DU, red M_{d} profile). Respective profiles of M_{d} fraction (thin red and green curves in b) are also shown. The Polly lidar observation was performed at Dushanbe on 13 April 2015, 16:15-16:44 UTC (white rectangle in Fig. 6). The temporally averaged lidar signal profiles were smoothed with 750 m before the computation of β_{p} and δ_{p}. Error bars indicate (a) 10% and (b) 30% uncertainty.

Atmos. Meas. Tech. Discuss., https://doi.org/10.5194/amt-2019-98
Manuscript under review for journal Atmos. Meas. Tech.
Discussion started: 14 March 2019

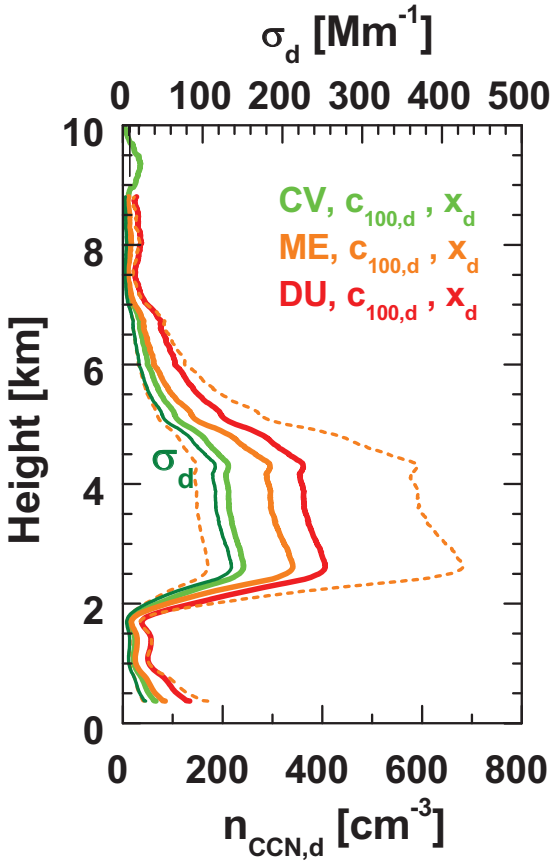

Figure 9. Estimation of dust CCNC profiles for the 16:15-16:44 UTC time period on 13 April 2015. The profile of the dust extinction coefficients σ_{d} (dark green) is converted into a profile of $n_{100,\mathrm{d}}$ by means the conversion parameters $c_{100,\mathrm{d}}$ and x_{d} given in Table 3 for Sal, Cabo Verde (CV, green profile), Mezaira (ME, orange profile), and Dushanbe (DU, red profile). For a typical water supersaturation value of 0.2% $n_{100,\mathrm{d}} \approx n_{\mathrm{CCN,d}}$. The uncertainty range is assumed to be of the order of a factor of 2 (indicated by dashed curves around the orange ME curve).

Atmos. Meas. Tech. Discuss., https://doi.org/10.5194/amt-2019-98
Manuscript under review for journal Atmos. Meas. Tech.
Discussion started: 14 March 2019

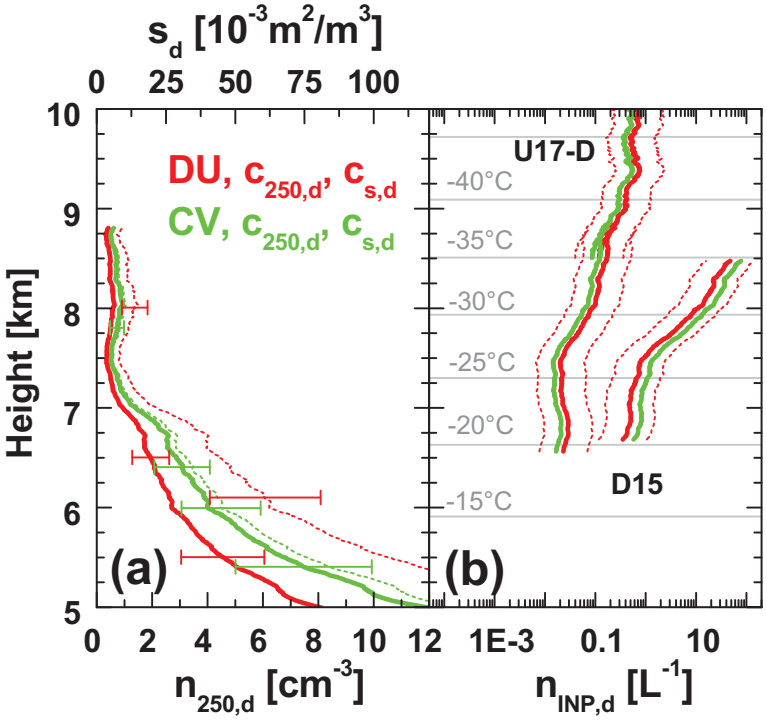

Figure 10. Estimation of INPC profiles for the 16:15-16:44 UTC time period on 13 April 2015. The profile of σ_{d} in Fig. 9 is converted into profiles of the particle number concentration $n_{250,\mathrm{d}}$ (thick solid lines in a) and surface area concentration s_{d} (thin dashed lines in a) by means of the conversion factors $c_{250,\mathrm{d}}$ and $c_{\mathrm{s,d}}$ in Table 3 for Dushanbe (DU, red profiles) and Sal, Cabo Verde (CV, green profiles). The profiles of $n_{250,\mathrm{d}}$ and s_{d} together with the actual temperature profile are input parameters in the INP parameterization schemes U17-D (deposition freezing) and D15 (immersion freezing, see Table 1). In the deposition-freezing INPC estimation, a typical ice supersaturation values of $S_{\mathrm{ice}} = 1.15$ is assumed. The INP parameterizations are valid for temperatures of about -20°C and lower. The D15 parameterization holds for temperatures down to -35°C only. Error bars indicate uncertainties of 30% in (a). The $n_{\mathrm{INP,d}}$ uncertainty range is one order of magnitude indicated by dashed lines in (b). We added $n_{\mathrm{INP,d}}$ profile segments for the 8.5-10 km height range, derived from lidar observations in cloud-free air from 15:15-16:10 UTC on 13 April 2015 (see Fig. 6).